Optical and structural characterization of (Mn, Fe) co-doped lead chalcogenides for optoelectronics applications

B. MERABET[a,b], O. M. OZKENDIR[c], A. S. HASSANIEN[d,e], M. A. MALEQUE[f,*]
[a]Faculty of Sciences and Technology, Mustapha Stambouli University, Mascara 29000, Algeria
[b]Computational Laboratory for Hybrid/Organic Photovoltaics (CLHYO) Istituto CNR di Scienzee Tecnologie Chimiche "Giulio Natta"(CNR-SCITEC) Via Elce di Sotto 8, 06123 Perugia, Italy
[c]Dept of Natural and Mathematical Sciences, Faculty of Engineering, Tarsus University, Turkey
[d]Faculty of Engineering at Shoubra - Cairo Benha university, Egypt
[e]Faculty of Science and Humanities, Afif, Shaqra University, Saudi Arabia
[f]Faculty of Engineering, International Islamic University Of Malaysia (IIUM), Malaysia

Lead chalcogenides (LCs) exhibit non-stability and lower device efficiency due to smaller bandgap (E_g) leading to poor optical properties for photovoltaic (PV) applications. In this work, optical properties of transition metals (TMs) such as (Mn and Fe) co-doped with LCs especially PbS in the framework of DFT+U (8 eV) and L/APW+*lo* method are theoretically investigated to predict new optical material for photovoltaic and other optoelectronics applications. The XAFS spectroscopy technique was used to analyze electronic structures and optical properties of (Mn, Fe) co-doped LCs. Midgap states of co-doped PbS reveal to improve the absorption of infrared light mainly due to slight doping with TMs. Compared to pure PbS, Mn doping in PbS induces E_g widening, blue-shift, and improve the light absorption edge. Due to co-doping, the magnetic order is translated that can lead to forming a charge compensated system which is beneficial to minimize vacancies related to defects formation.

1. Introduction

The breakthrough of wide bandgap (E_g) semiconductors have gained interest to lowering carbon footprints in buildings via clean renewable energies converted to electricity for industrial production and household applications [1-3]. Due to broad absorption spectra, narrow emission spectra, high charge carrier mobility, and multiple exciton generation capability, chalcogenides are stunning absorbers for photovoltaic (PV) applications on account of their uniquely high absorbance and broad-band absorption [4-6]. Beside their use in tunable laser devices [7], lead chalcogenides (LCs) such as PbS, have attracted much attention for their ease of synthesis, commercial availability [8], and potential applications in sensors 9-11], bio-electronics [12], solar cells (SCs) [13-18], and thermoelectric cooling materials [19-21], due to their high carrier mobility and low lattice thermal conductivities [22-25]. The p-type hole transporting layer for planar of Sb_2Se_3SCs and PbS is used to minimize the carrier recombination loss at back contacts, and boost the carrier transport efficacy [24], moreover, PbS base device can outperform in all alternatives due to excellent properties of Pb [25]. However, LCs for PV cells application have found difficulty due to non-stability, toxicity and lower device efficiency [26], while PV devices are challenged to exploit new, stable, and low-cost of present-day materials [27].

Doping the paramagnetic PbS with paramagnetic ions of transition metals (TMs) such as Mn^{2+} and Fe^{2+}, however,

reveals to adapt its physical properties mainly in nanostructures for the application of photonic and spintronic devices [28-30]. The characteristics of the optical absorption and glass transition temperature of As-Se, As-Se-S, As-Se-Te LC semiconductors has been explained [31]. From the photomagnetic properties of TM-doped PbS prominent features can be emerged [32]. The bandgap (E_g) engineering [33] of co-doped PbS can provide offers a large properties for tunability in infrared (IR) band and visible range resulting better transparent of doped PbS [34]. Generally, PbS with high absorption coefficient is used in IR detectors [35]. To improve open-circuit voltages (V_{OC}), it is important to enhance power conversion efficiencies (PCE) of LCs for SCs application, which is possible by introducing dopants such as TM ions which will create midgap states (MGSs) and change the charge separation/recombination dynamics [36]. Extensive research works have been reported on doping effects in MT chalcogenides. The Mn-doped CdS by Wu et al. [37] found that Mn^{2+} cations could create MGSs allowing the generation of long-lived charge carriers. As for Fe-doped CdS, Chauhan et al. [38] reported that Fe^{2+} cations doping CdS could increase the lifetime of excited charge carriers, and enhance the photocatalytic activity. Mahboub et al. [39] reported that the saturation of MGSs minimizes traps detrimental to charge transport in Cd^{2+}/ Zn^{2+} treated-PbS with cations enhancing PCE. Blackburn et al. [40] however, revealed that MGSs can dissociate excitons by trapping charge carriers, and play a beneficial role in tuning band energetics or providing catalytic sites [41].

Also, the intrinsic toxicity of Cd/Pb chalcogenides and potential exposure of such materials to the eco-system may pose momentous threats to the environment [5]. It is unclear whether the midgap carrier trapping the limit of V_{OC} in LCs for SCs [3, 14] or MGSs improve it with doping [36, 42]. An increase in the optical E_g of PbS due to quantum confinement effect can lead to E_g tuning with MT doping, and make it worthy for tunable optoelectronic devices [43]. Therefore, the aim of this study is to investigate the optical properties of (Mn, Fe) co-doped LCs to find the relationship between MGSs and (Mn, Fe) co-doped PbS systems for PV and other optoelectronics applications.

2. Theoretical method

Density functional theory (DFT+U)(8 eV) framework was implemented whereby atoms are represented by the augmented plane wave method at full hybrid potential (linear), including local orbitals (L/APW+lo) [44].Wave functions, charge density and potential are extended in spherical harmonics in no Muffin-Tin (MT) sphere overlaps, and plane waves are used in the remaining interstitial region of the unit cell. Core and valence states are treated respectively by Dirac-Fock's multi-configuration relativistic approach and scalar relativistic approach. For the exchange-correlation energy, GGA+U approach was used [45]. To overcome the underestimation of E_g due to GGA approximation, the modified Becke-Johnson potential approximation (mBJ) was employed. An accurate set of k-points was optimized in order to ensure the convergence of the total energy in terms of the cutoff-energy variation parameter. Equilibrium constants and compressibility moduli were calculated and fitted according to Murnaghan's equation, [46] and minimized using a set of 10 k-points in the irreducible Brillion Zone (BZ), equivalent to a Monkhorst-Pack [47] grid of 6×6×6 in the unit cell; a value of 7 Ry as cut-off energy was used. Self-coherent calculations are considered convergent only when total calculated energy of the crystal converges to less than 1 mRy, adopting the appropriate MT Radii. Density of the states (DOS) was calculated using the linear tetrahedron method with Blöchl corrections [48]. Calculations were carried out using a 64-atoms supercell in the Fm3m symmetry. The exchange-correlation energy was calculated using GGA+(U of 3.4eV) [45] approach. Basic standard built-in functions are applied for Pb, S, Mn and Fe valence configurations using $5s^2 5p^6 4f^7 5d^1 6s^2$, $5s^2 5p^6 4f^{11} 5d^1 6s^2$, $5s^2 5p^6 4f^{14} 5d^1 6s^2$ and $3s^2 3p^6 3d^3 4s^2$, respectively. A set of 163 k-points mesh in the irreducible ZB was used for $Pb_{0.25}Mn/Fe_{0.25}S$ and $Pb_{0.25}Mn_{0.125}Fe_{0.125}S$.

3. XAFS characterization

An X-ray absorption fine structure (XAFS) characterization was performed for the electronic response (electron transfer) of both Mn and Fe substitutions in the lead (Pb) coordination. The calculations was performed for Mn or Fe substitution or both at the same time via the general formula "$Pb_{1-y}(Mn_{1-x}Fe_x)_yS$" with the variants of: y=0.05, 0.10, and 0.20, while x= 0.0, 0.5, and 1.0. The calculations were carried out with FEFF 8.2 program, which is one of the most reliable codes that can be employed with the XAFS technique [49]. XAFS spectroscopy can provide detailed information about the electronic structures and crystal coordination of atoms to investigate the electronic structures of atoms, properties of valence electrons, bond structures, as well as atomic configurations within the crystal. For the electronic properties of materials, the inner shell ionization process was considered by the XANES spectroscopy which contains rich data in its spectrum. On the XAFS spectra of an interested material, the XANES spectra lays between 20 eV below and 50~70 eV above the main absorption edge. Beyond the XANES spectrum, the tail spectrum lays where spectral fluctuations take place as an indication of the interruption of the excited photoelectrons' travel between high kinetic energies and atoms with continuous scattering. This high energy part of the spectrum is called the expanded XAFS (EXAFS) region with an energy range of 400~800 eV. The oscillation observed in this section is related to the arrangement of atoms, i.e., it carries information about the configurations of neighboring atoms, atomic distances and coordination numbers [50]. In addition, full multiple scattering calculations were performed by the real-space multiple scattering approach at room temperature (~300 ^{0}K) using the FEFF8.20 code [50]. The input files for the calculations of the $Pb_{1-y}(Mn_{1-x}Fe_x)_yS$ material series, a lead (Pb) and sulfur (S: for the second round of calculations) atom was selected as the source atom which is located at the origin in real space. For the calculation, the first input file was prepared for 10 Å thick Pb atom as a reference material in cubic fcc with "$Fm3m$" geometry containing 141 atoms with the lattice parameters of a: 4.950 Å and Pb (x,y,z): (0.0, 0.0, 0.0). The second input file was prepared for the 10 Å thick PbS material with cubic "$Fm3m$" geometry containing a cluster of 171 atoms. Crystal parameters of PbS material were a: 5.934Å; Pb^{2+}(x,y,z): (0.0, 0.0, 0.0), S^{2-} (0.5, 0.5, 0.5). Mn and Fe TM atoms were relocated in lead coordination randomly with the substituted amounts of PbS material. Input data files were generated according to the general formula of $Pb_{1-y}(Mn_{1-x}Fe_x)_yS$; ($y$, x) couples of:(0.05, 0.00)→$Pb_{0.95}Mn_{0.05}S$; (0.05, 0.95)→$Pb_{0.95}Fe_{0.05}S$; (0.10, 0.00)→ $Pb_{0.90}Mn_{0.10}S$, $Pb_{0.90}Fe_{0.10}S$ and $Pb_{0.90}Mn_{0.05}Fe_{0.05}S$; and (0.20, 0.00)→$Pb_{0.80}Mn_{0.20}S$ and $Pb_{0.80}Fe_{0.20}S$. For the calculation of S atom, a pure S cluster was obtained as a reference for the orthorhombic geometry with *fddd* space group. Lattice parameters of S atoms are: a: 10.467Å; b: 12.870Å; c: 24.493 Å, and α=β=γ=90°.

4. Results and discussions

4.1. Electronic structure and magnetic order

Doping LCs, having gained much attention for ease of synthesis, commercial availability, and potential applications, with impurities alter the energy levels of the valence band (VB) and/or the conduction band (CB) leading to the widening or narrowing of E_g [51]. Fig. 1 shows DFT electronic band structure of $Pb_{0.25}Mn_{0.125}Fe_{0.125}S$. PbS exhibited a direct gap and E_g varied in a wide range from

0.41 eV at 300^0K to 2.3 eV, [52] but in this study it was found to be 0.822 eV which is much lower than those obtained from Mn-doped PbS and (Mn, Fe)-codoped PbS and estimated as 1.042 and 0.982 eV, respectively. VB max (VBM) and CB min (CBM) of (Mn, Fe)-codoped PbS occurred at the Γ-point instead of L-point of PbS. This is due to moving or shifting of the spectra along the Λ-Γ line of the top valence band (VB) and shifting of the Fermi level (E_F). It was noticed that a sizable splitting exits between the

bonding and anti-bonding bands of (Mn, Fe)-codoped PbS bands [53], within a very small value of 25meVat E_F along the same line. This E_F band shifting which is closed to Γ point gives rise to a small hole pocket as well [54]. In terms of degeneracy, fivefold degeneration of TMs at $3d$ states are occurred which splits into three fold low-lying t_{2g} and twofold high-lying e_g subsets due to the octahedral crystal field of O_h.
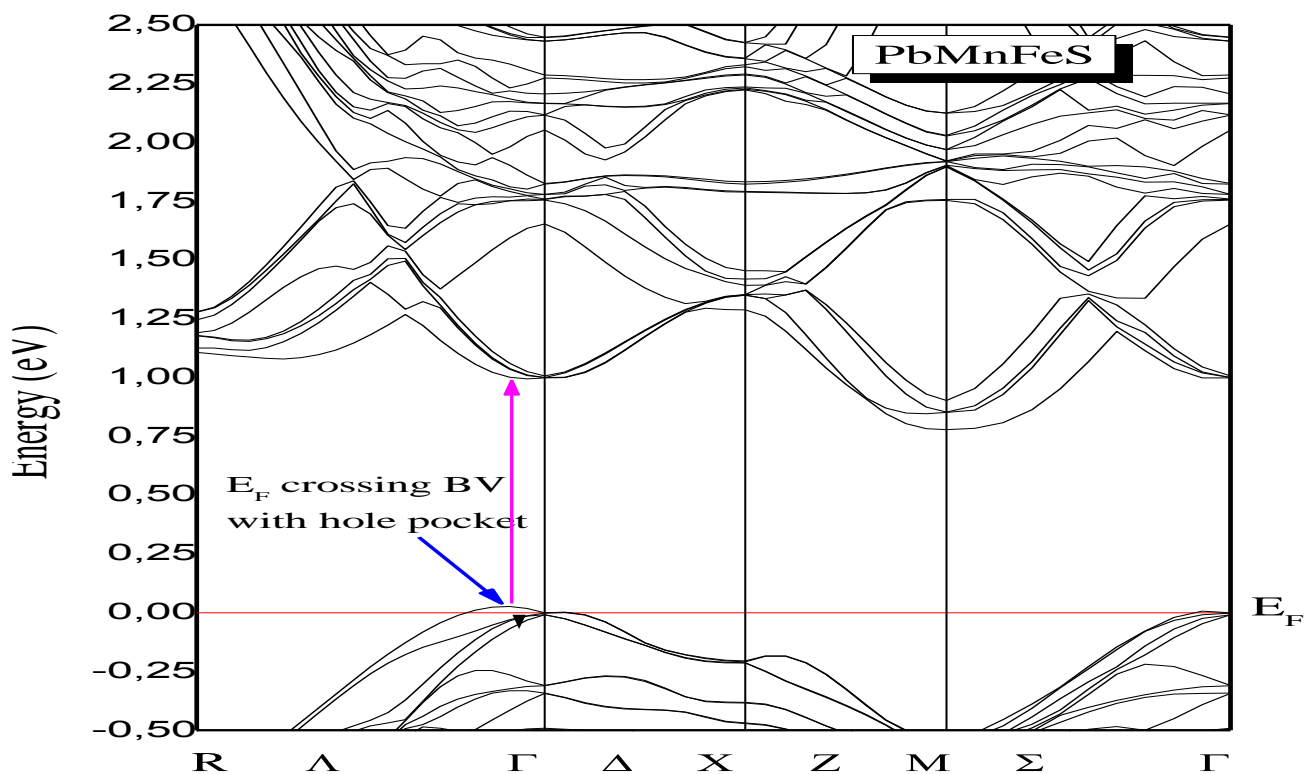

Fig. 1. Electronic band structure of $Pb_{0.25}Mn_{0.125}Fe_{0.125}S$. A very clear E_F crossing is seen close to Γ_1 towards Δ of BZ, and a hole pocket has to be mentioned. For optoelectronic applications, vertical optical transitions are noticed (color online)

The dielectric function, ε(ω) reflects the band structure and spectral information of a solid and establishes a relationship between its electron structure and electron transitions from microscopic processes. Fig. 2 shows partial and total densities of states (P/T-DOS) of (Mn, Fe)-doped PbS, whereby TM dopants (Mn and Fe) donating two electrons to Pb site in order to form anion dangling bonds resulting in $3d^5$ and $3d^6$ configurations for Mn^{2+} and Fe^{2+}, respectively. It can be seen that the top of BV (right side of Fig 2) is dominated by (Mn, Fe)-d S-p states with slight contribution of Pb-s state, while Pb-s states possess the same symmetry as VB at Γ-point leading to the strong level-repulsion and pushes S-p states upward direction. The up-

spin t_{2g} states and gradually up-spin e_g states increased d-electrons resulting increased in M_{tot} value of 4.999 and 4.002 μB for TMs (Mn, Fe) dopants and (Mn, Fe)-codoped PbS, respectively.

Fig. 3 shows real ($ε_1$) and imaginary ($ε_2$) of dielectric functions for $Pb_{0.25}(Mn, Fe)_{0.25}S$ and $Pb_{0.25}Mn_{0.125}Fe_{0.125}S$. When introduces Mn and Fe dopants, they significantly affect the static ε(ω) and peak become smaller for Mn- and Fe-doped PbS compared to the (Mn, Fe)-codoped PbS. The $ε_1$(ω) of Mn-, Fe-doped and (Mn, Fe)-codoped PbS are demonstrated energy band over (3.76-7.73), (4.01-10.39) and (3.84-8.59)eV, respectively indicating that photons in these ranges cannot travel in the medium.
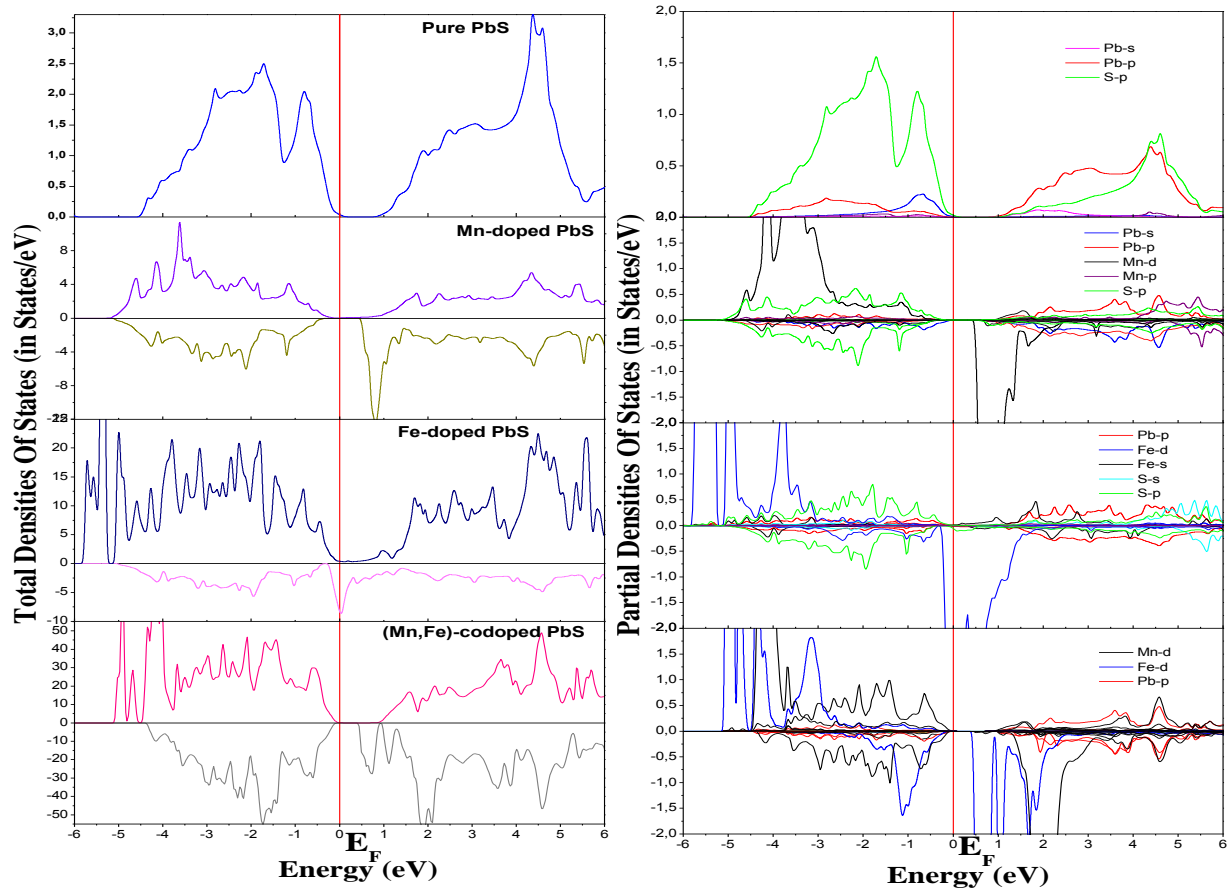
Fig. 2. Total and partial densities of states (T/P-DOS) of $Pb_{0.25}(Mn/Fe)_{0.25}S$ and $Pb_{0.25}Mn_{0.125}Fe_{0.125}S$ (color online)
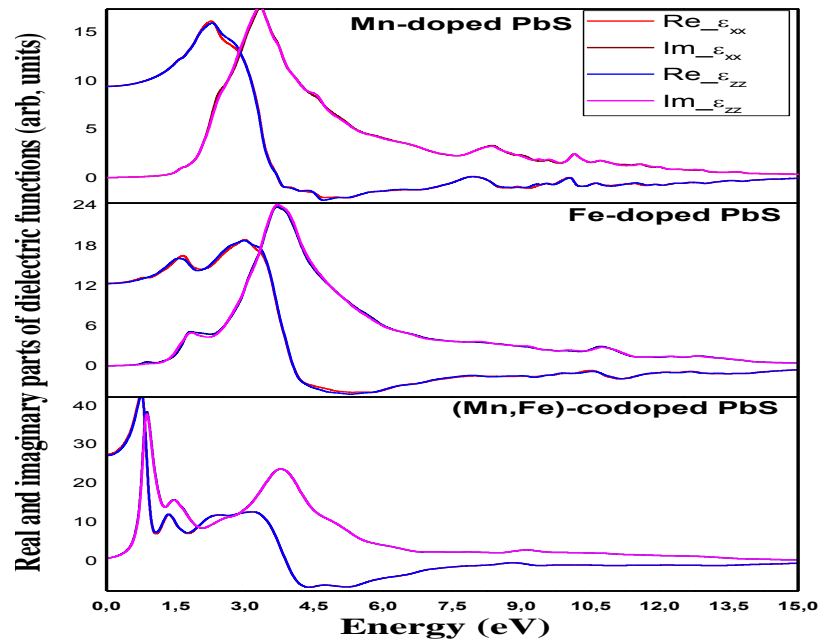

Fig. 3. Real (ε_1)and imaginary(ε_2) of dielectric functions for$Pb_{0.25}(Mn, Fe)_{0.25}S$ and $Pb_{0.25}Mn_{0.125}Fe_{0.125}S$ (color online)

However, Mn and (Mn, Fe) dopants have similar effects on negative value of real dielectric functions (ε_1) compared to that of Fe dopant. In this case, Fe^{2+}/Mn^{2+} ions might assist in electron accumulation for shifting E_F to cross the VB (as shown in Fig. 1).

In real application, this nature can influence charge carrier generation and recombination of LCs-based SC. The $3d$ TMs dopants in LCs (PbS) produced high spin polarization for Mn-doped PbS,Fe-doped PbS and (Fe, Mn)-codoped PbS which maintain the semiconductor

characteristics of the materials with a small E_g widening and is worthy to be taken into account for further tuning of other physical properties of the materials. A strong hybridization between dopants and neighboring S orbitals (mainly, Fe-3d/S-4p) was observed in this study. The spin-orbital coupling between Mn-3d and S-4p or Fe-3d and S-4p states was very weak leading to the antiferromagnetic (AFM) coupling behavior of the material. Moreover, both Mn- and Fe-doped PbS compounds exhibited an AFM order, while a nonmagnetic (NM) state was predicted with (Mn, Fe)-codoped PbS. Therefore, it is revealed that the codoping in PbS can easily tailor the magnetism properties of new material with 3dTM atoms. It was also confirmed by previous finding [55] whereby doping on magnetic properties of SnS monolayer were studied. Paramagnetic characteristics of PbS revealed in the codoped system whereby d-electrons interacted with Mn-/Fe- spins which naturally enhance the optical properties in presence of dopants [56]. This dual functionality of this codoped material stimulates to select this type of LCs material for SCs and other spintronic applications.

4.2. Optical properties of LCs

Defect states play a key role in determining optical properties of LCs whereas, defect state engineering provides a pathway to develop SCs [31]. Given the interest of LCs as potential light harvesters, particular attention to optical E_g engineering is focused. Moreover, defect states energy and density enhance the optical property of these materials. For instance, Mn-doped CdS showing emission at ~585 nm due to the Mn $d-d$ transition which can be explored to design high efficiency SCs. The optical properties of Mn-, Fe-doped PbS and (Mn, Fe)-codoped PbS were investigated via dielectric functions as shown in

Fig. 4. Compared to pure PbS, Mn-doped PbS induces an E_g widening with the increasing of the exciton recombination energy and a blue-shift on tuning the optical window between 2870 and 890 nm. Moreover, optical E_g for Fe-doped PbS is also blue shifted with Fe doping following the enhancement of magnetic properties [57]. With the limit of $E(eV) \geq 1240 / \lambda(nm)$, $Pb_{0.75}(Mn, Fe)_{0.25}S$, and $Pb_{0.25}Mn_{0.125}Fe_{0.125}S$ absorption edges are estimated to be wavelengths of around 890/950 and 2870 nm, respectively (the optical bandgaps are mentioned in blue arrays in Fig. 4.b). Codoping PbS with (Mn, Fe)-MTs leads to significant effects on the optical absorption in wavelength ranges longer than 890 nm, giving rise to the absorption edge shift of this material. As mentioned earlier, optical E_g for codoped PbS slightly blue shifted with Fe^{2+} and Mn^{2+} ions due to Burstein-Moss effect [58]. From Fig. 4 (a), which represents optical real conductivities, $\sigma(\omega)$ vs energy, it can be seen that several peaks correspond to the bulk plasmon excitations due to the electrons crossing from VB to CB. Between high energy range of more than 5 eV and low energy range of 0.48-4.34 eV, $\sigma(\omega)$ correspond to interband and intraband transitions, respectively. For all doped and codoped PbS compounds, single sharp peak over low energies and several small peaks over high energy ranges are obserbed, beside main peaks localized at 3.43, 3.84 and 3.91 eV for Mn-, Fe-doped and (Mn, Fe)- codoped, respectively. For all compounds, $\sigma(\omega)$ is very small over visible wavelengths, and increases sharply beyond 890 nm at excitation energies above E_g, in parallel with the absorption edge of the PbS compounds and confirms formation of electron/hole pairs when energy is $h\upsilon \geq E_g$ (with h Planck' constant and υ the excitation frequency).
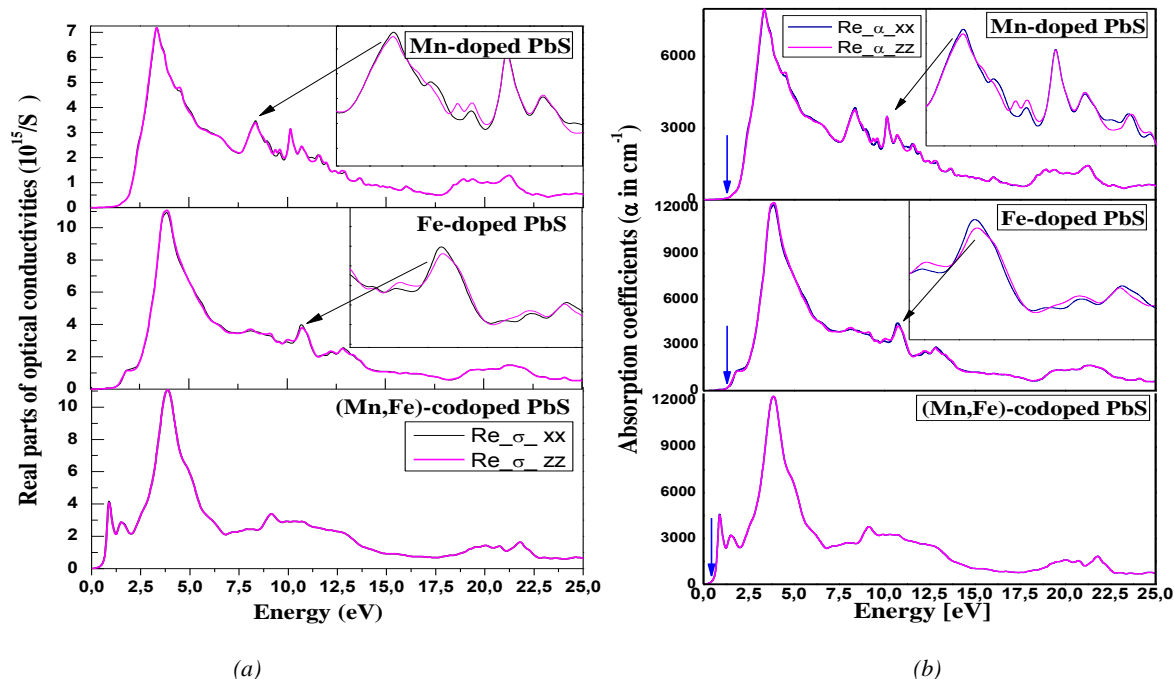

(a)   *(b)*

Fig. 4. (a) Optical real conductivities (σ^{xx}, σ^{zz}) and b) Absorption coefficients (α^{xx}, α^{zz}) ofPb$_{0.25}$(Mn/Fe)$_{0.25}$S and Pb$_{0.25}$Mn$_{0.125}$Fe$_{0.125}$S (color online)

Comparing Mn-, Fe-doped PbS and with (Mn, Fe)-codoped PbS, it can be noted that the dielectric absorption within low energy range is mainly enhanced by Fe-dopant, whereas, the absorption coefficient of PbS enhanced by TM (Mn, Fe) atoms in blue light range.The main absorption peaks are produced at 3.41 and 3.85 eV for Mn and Fe dopant, respectively. A less sharp peak was observed near the optical bandgap energy (E_g) of 0.96 eV in presence of (Mn, Fe) dopant. This could be attributed from the electron transition between MGSs level and the top of BV. In a nutshell, the optical spectrum depicted that the absorption peak of (Mn, Fe)-codoped PbS is extended to the visible region due to narrowing of the band gap to 2.67 eV.

4.3. Crystal structure

Fig. 5. shows XANES spectra of PbS, Mn- and Fe-dopant in PbS and (Mn, Fe)-codoped PbS whereby Pb L_3-edge spectrum is the reference spectrum. L_3-edge was selected for full multiple scattering calculations based on high sensitivity for the core inner shell excitation process in the lead atoms. The Pb was selected as a reference which demonstrates the influence of S on the electronic and crystal structure of lead atoms. In this case, L_3-edge absorption spectra is a result of excited electrons' transition from $2p_{3/2}$ level as the initial state to unoccupied level over E_F as the

final state. However, the transitions are limited by the quantum dipole selection rules whereby excited electrons are participated during the relocation process. The electronic configuration of lead is $4f^{14}5d^{10}6s^26p^2$ and when form a compound with sulfur (PbS), the configuration of Pb^{2+} ions become $4f^{14}5d^{10}6s^26p^07s^5f6d^{10}$. Therefore, the dipole selection rules are limited to the possible final state by $\Delta l = \pm 1$. Thus, in the final state, the 2p electrons could not unoccupied at $6p$ level, rather $7s$ level.

From Fig. 5, it can be seen that PbL_3-edge spectrum has similar edge feature with PbS, Mn-and Fe-doped PbS materials. This similarity behavior represents similar crystal properties of both materials with the same cubic "*Fm3m*" geometry. However, it is also noticeable that Pb absorption spectra has separated from other spectrum due to the ionic state of Pb^{2+} in PbS. Moreover, L_3-edge spectrum for both samples (with Mn and Fe in PbS) have started increasing at the energy of 13035.4 eV and given a weak narrow edge structure at 13044.6 eV. The same peak structure has appeared on the Pb spectra at the energy of 13046.1 eV with a 1.5 eV shift due to the ionic state of the lead atoms in the PbS structure. The narrow peak "A" (in Fig. 5) addresses the $2p_{3/2}$ electron's transition to unoccupied $7s$ levels which is above the unoccupied $6p$ levels following the dipole selection rule.
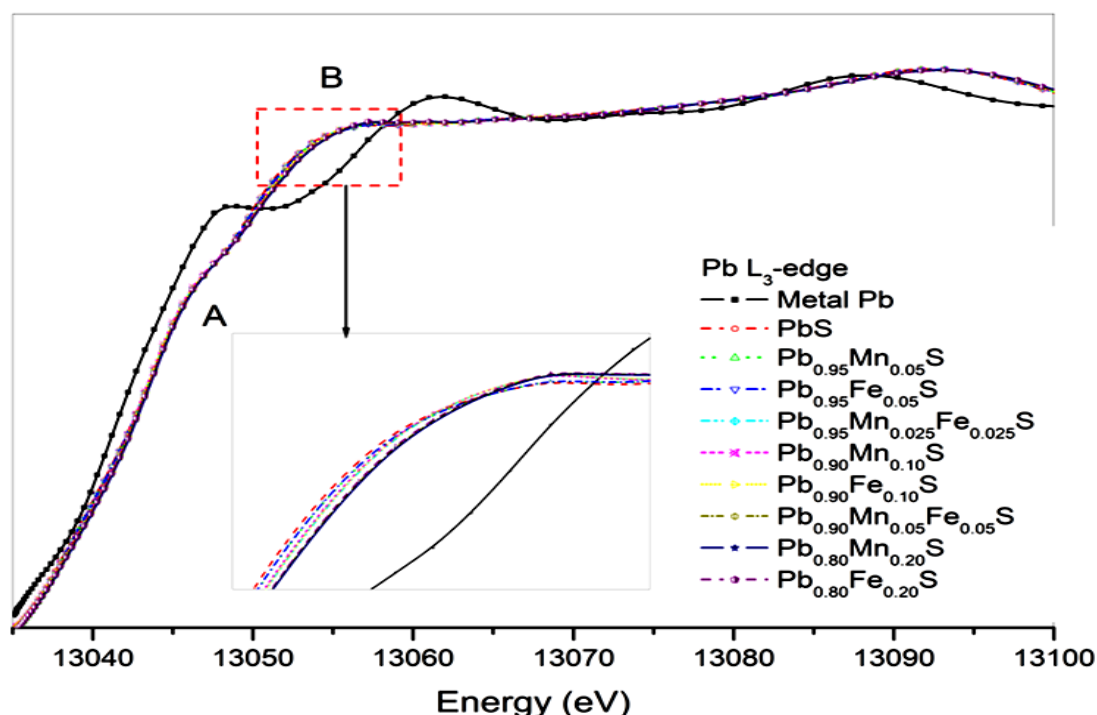

Fig. 5. XANES spectra of PbS, Mn- and Fe-dopant in PbS and (Mn, Fe)-codopedPbS. Here Pb L₃-edge spectrum is the reference spectrum (color online)

Broader absorption peak structure demonstrates broader electronic levels that provide convenient holes for the excited p-level electrons. Referring to the broader peak "B" in Fig 5, this phenomenon is happed due to the electronic transitions from p-level to the unoccupied 6d

levels whereby the peak has a maximum value of energy 13056.2 eV compared to Pb which has a maximum value of 13061 eV. The energy difference and the shift at PbS series are a result of the unoccupied np levels during the ionization. Therefore, L_3-edge spectra of the PbS and (Mn,

Fe)-codoped PbS series are in agreements with the above statement for spectral features also can be concluded that Mn and Fe atoms are highly fit with atomic environment of lead for the development of new materials.

It is worthy to mention that Mn and Fe atoms are located in Pb coordination (as shown in Fig. 5) without any process and hence, S would give a better approach to the doping process which can greatly influence the dopants (Mn, Fe) on its environment. Fig. 6, shows k-edge XANES spectrum of pure S, PbS, Mn- and Fe-dopant in PbS and (Mn, Fe)-codoped PbS whereby S K-edge spectra is the reference spectra.
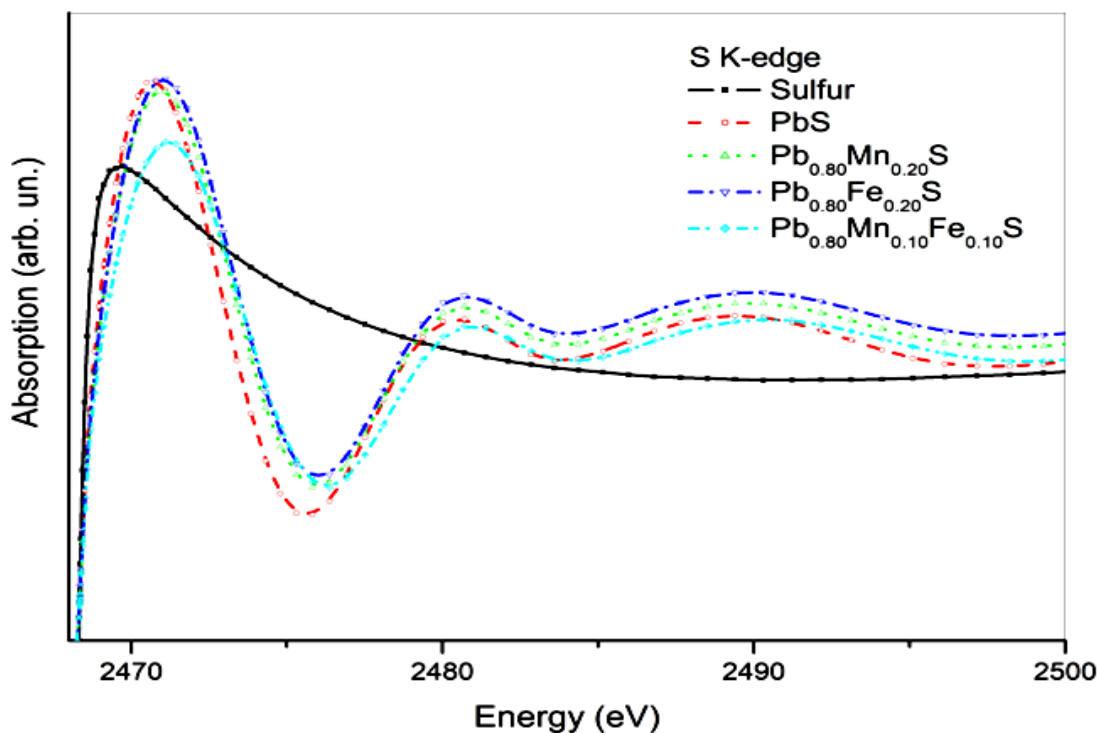

Fig. 6. K-edge XANES spectrum of pure S, PbS, Mn- and Fe-dopant in PbS and (Mn, Fe)-codopedPbS. Here, S K-edge spectra is the reference spectra (color online)

Fig. 7 depicts the scattering intensity of pure S, Mn-, Fe-dopants and (Mn, Fe)-codoped PbS. The scattering intensity of Pb atoms demonstrates higher scattering intensity at higher k-value in which strong scattering process occurred in the vicinity of the Pb atoms. However, the shifting of the scattering intensity for PbS, Mn-, Fe-doped PbS and (Mn, Fe)-codoped PbS materials are the results of S, Mn, and Fe atoms presence in the structure whereby Pb atoms cluster have only one type of atom in the crystal. Thus, it represents heterogeneous peak features of scattering data for the PbS and (Mn, Fe)-codoped PbS samples and are due to the presence of different type of atoms in the bulk.

The scattering data of the samples also shows the decay at lower k value, *i.e.* longer mean free path (k~1/l). Apart from the Pb cluster, the scattering intensities of the doped and codoped materials have also strong peak structures between 3-9k values which are heavier than S and increases the interstitial potential of PbS parent material but decrease the photoelectrons' kinetic energy. The change of peak structure with Mn and Fe atoms are given in the inset with a magnified scattering peak. The Fourier Transform (FT) of the scattering data yields the atomic displacements where photoelectrons scattering interactions occur. Thus, the FT of the EXAFS scattering data was performed to determine the atomic distances from the source atoms which is also known as Radial Distribution function (RDF).
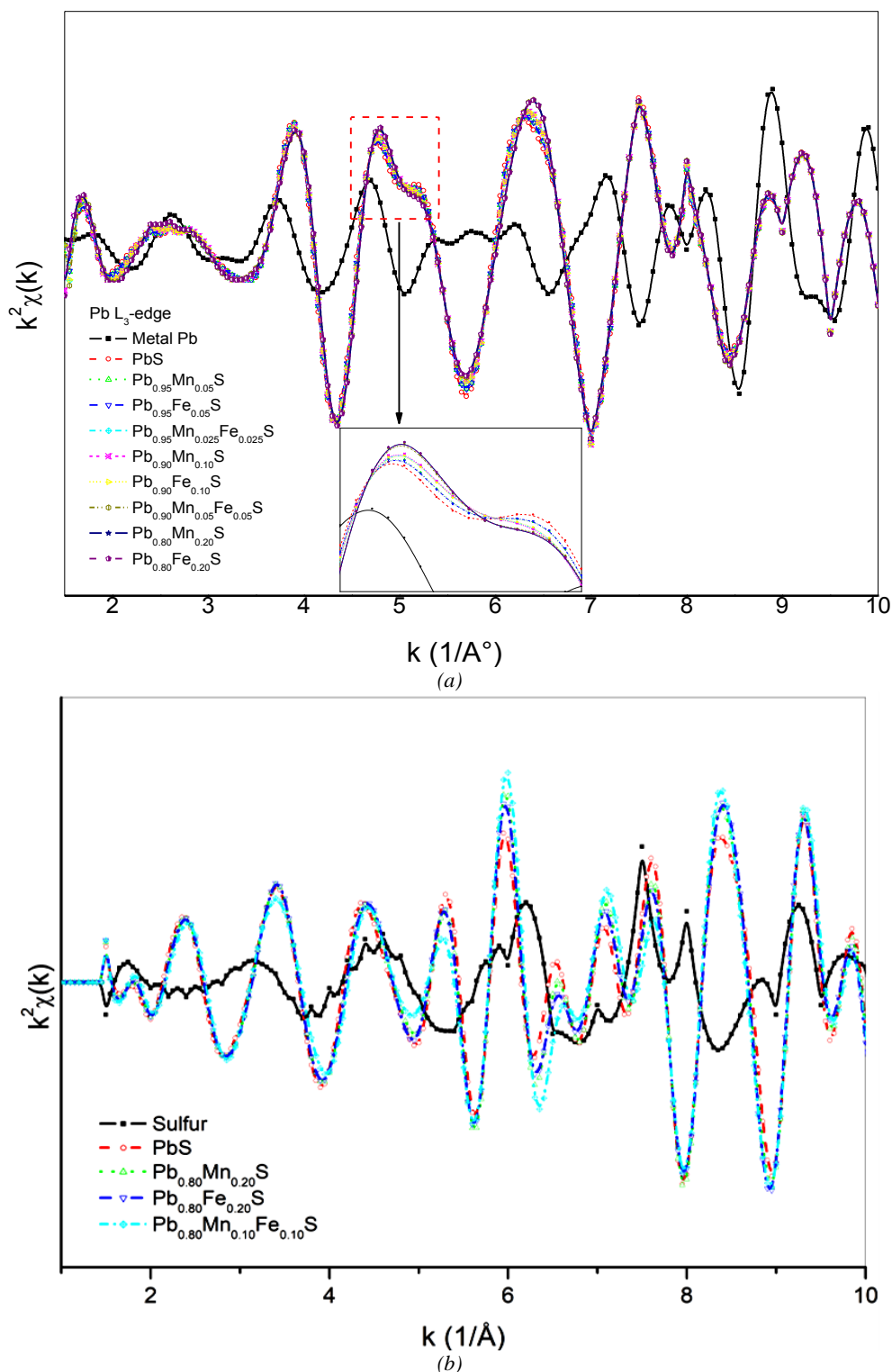
Fig. 7. The scattering intensity of pure S, Mn-, Fe-dopants and (Mn, Fe)-codoped PbS: a) based on Pb atoms; b) based on S atoms (color online)

Fig. 8 shows the RDF of PbS, Mn-, and Fe-doped PbS whereby S is in the origin can greatly influence the dopants (Mn, Fe) on its environment. The RDF data were yielded from the scattering data of S atoms as shown in Fig. 7.*b*. The symmetry of atomic peak distance indicates the electronic adaptation of both Mn and Fe atoms that do not alter the electronic structure in lead atoms environment. Therefore, this symmetry demonstrates the stable crystal structure of new material around S atoms in PbS compound.
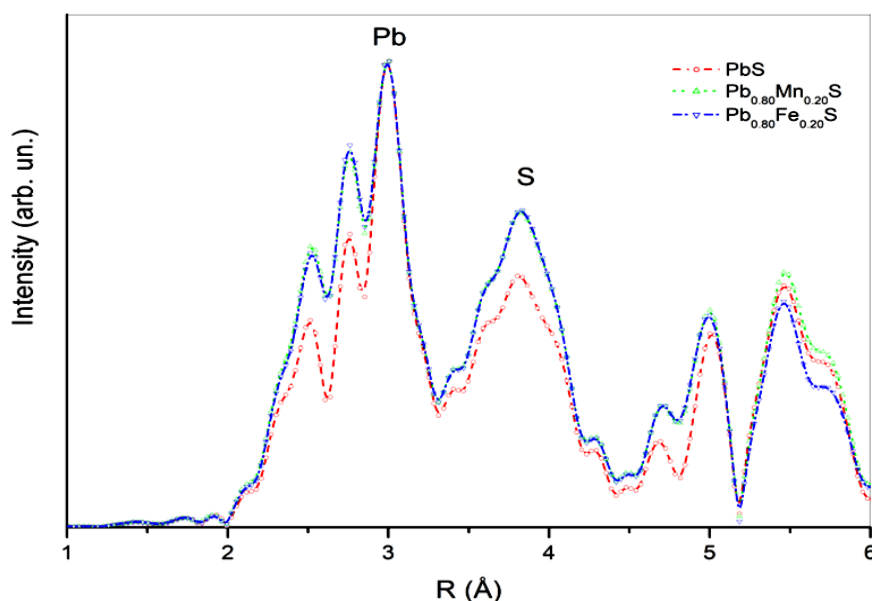
Fig. 8. Radial distribution function of PbS, Pb$_{0.80}$(Mn, Fe)$_{0.20}$S samples; S atom is sitting at the origin (color online)

The closest atomic distance of PbS was determined as the closest atomic shells with Debye-Waller (s^2) factors such as, 6 Pb atoms and (S-Pb) at a distance of 2.967 Å and closest S shell (S-S) at a distance of 2.967 Å with s^{2}of 0.00531 Å^2.The multiple peak features on the same body of the RDF peaks are due to the angular differentiation of the atoms on the axis scales. Pure S has an electronic configuration of 3s^2 3p^4, but in the PbS material it becomes 3s^2 3p^6 totally occupied levels and shares two electrons for bonding with Pb atoms. Thus, the k-edge XANES spectra of pure S has a strong and narrow edge structure of 1s→3p transition after following dipole selection rule.

However, for the PbS material, the *p*-level is occupied and the close peak energy of the S k-edge addresses the transitions to the 3*ps** anti-bonding levels on S atom. The k-edge absorption spectra of S atoms has increased to 2466 eV and reached to a maximum of 2469.6 eV for pure S atom and 2470.6eV for S atom in PbS atoms. However, with Mn-dopant, the peak energy has shifted to higher energy of 0.3 eV and with Fe-dopant increased the value to 0.7 eV. The peak energy shift emphasizes the interaction of both Mn and Fe atoms with S atoms.The same result has also presented in the inset of Fig. 5 for Pb L$_3$-edge. According to Fig. 6 and the inset in Fig.5, the dopant has caused a narrowing in the Pb atoms electronic levels while a broadening in S atom levels that confirms the electron gain of S during molecular bonding.The current also highlighted that the doping process and its influence on the PbS crystal can be traceable with XANES and XAFS data processing whereby the scattering data of the PbS atoms were extracted from the XAFS tail spectra.

5. Conclusion

In summary, the electronic structure of Mn-, Fe-doped PbS and with (Mn, Fe)-codoped PbS were analyzed by XAFS spectroscopy technique, and optical properties of these materials (LCs with doping of TMs) are theoretically investigated. The paramagnetic order turns into AFM for Mn-, Fe-doped or (Mn, Fe)-codoped PbS. Fe doping enhances the dielectric absorption while Mn incorporation creates midgap states and allows the generation of long-lived charge carriers. The codoping process with (Mn, Fe) in PbS leads to E$_g$ blue shift, and tailors the magnetism with 3*d*TM atoms. The absorption in visible light and infrared light ranges has been largely improved due to the introduction of (Mn, Fe)-codoped material. This study contributes to understand optical and structural properties of LCs with dual functionality stimulating further study for photovoltaic and optoelectronics applications.

References

[1] I. Kim, K. Kim, Y. Oh, K. Woo, G. Cao, S. Jeong, J. Moon. Chem. Mater. **26**(13), 3957 (2014).
[2] S. Chu, C. N. Liu. Nat. Mater. **16**, 16 (2017).
[3] A. Hajijafarassar, F. Martinho, F. Stulen, S. Grini, S. López-Mariño, M. Espíndola-Rodríguez, O. Hansen, Sol. Energy Mater Sol. Cells **207**, 110334 (2020).
[4] A. J. Nozik, M. C. Beard, J. M. Luther, M. Law, R. J. Ellingson, J. C. Johnson. Chem. Rev. **110**(11), 6873 (2010).

[5] H. Fu, Mater. Chem. C **6**, 414 (2018).

[6] T. L. K. Pralay, S. P. V. Kamat. J. Am. Chem. Soc. **135**(2), 877 (2013).

[7] Y. L. Pei, Y. Liu. J. Alloys Compd. **514**, 40 (2012).

[8] O. P. Garcia, M. C. C. Albuquerque, K. A. Aquino, P. L. B. Araujo, E. S. Araujo. Mater. Res. **18**(2), 365 (2015).

[9] S. J. Oh, N. E. Berry, J.-H. Choi, E. A. Gaulding, T. Paik, S. H. Hong, C. R. Kagan. ACS Nano **7**(3), 2413 (2013).

[10] D. V. Talapin, C. B. Murray. Science **310**, 86 (2005).

[11] W. Koh, S. R. Saudari, A. T. Fafarman, C. R. Kagan, C. B. Murray. Nano Lett. **11**, 4764 (2011).

[12] A. Shrestha, M. Batmunkh, A. Tricoli, S. Dai, S. Z. Qiao. Angew. Chem. **58**(16), 5202 (2018).

[13] H. Fu, S. W. Tsang. Nanoscale **4**, 2187 (2012).

[14] D. M. Balazs, M. A. Loi, Adv. Materials **30**(33), 1800082 (2018).

[16] F. Bertolotti, D. Dirin, M. Ibáñez. Nature Mater. **15**, 987 (2016).

[17] J. H. Rhee, C. C. Chung, E. W. G. Diau. NPG Asia Materials **5**(10), 68 (2013).

[18] Z. Pan, I. Mora-Seró, Q. Shen, H. Zhang, Y. Li, K. Zhao, J. Bisquert, J. Am. Chem. Soc. **136**(25), 9203 (2014).

[19] R. Y. Wang, J. P. Feser, J. S. Lee, D. V. Talapin, R. Segalman, A. Majumdar, Nano Lett. **8**, 2283 (2008).

[20] Y. Hou, H. Kondoh, T. Ohta, Crystal Growth & Design **9**(7), 3119 (2009).

[21] E. Hazan, O. Ben-Yehuda, N. Madar, Y. Gelbstein, Ad. Energy Mater. **5**(11), 1500272 (2015).

[22] K. Kurosaki & S. Yamanaka, Physica Status Solidi A **210**(1), 82 (2012).

[24] S. A. Yamini, D. R. G. Mitchell, Z. M. Gibbs, R. Santos, V. Patterson, S. Li, S. G. Jeffrey, Adv. Energy Mater. **5**(21), 1501047 (2015).

[25] M. Oudah, K. M. Kleinke, H. Kleinke, Inorg. Chem. **54**(3), 845 (2015).

[26] C. Chen, L. Wang, L. Gao, D. Nam, D. Li, K. Li, Y. Zhao, C. Ge, H. Cheong, H. Liu, H. Song, J. Tang, ACS Energy Lett. **2**, 2125 (2017).

[27] A. M. Ganose, C. N. Savory, D. O. Scanlon, Chem. Commun. **53**, 20 (2017).

[28] I. V. Fernández, S. Mariotti, O. S. Hutter, M. Birkett, T. D. Veal, L. J. Phillips, Chem. Mater. **32**(15), 6676 (2020).

[29] H. Lei, J. Chen, Z. Tan, G. Fang, Solar RRL **3**, 1900026 (2019).

[30] M. Suganya, A. R. Balu, D. Prabha, J. Mater. Sci.: Mater. Electron. **29**, 1065 (2018).

[31] R. I. Alekberov, I. Isayev, S. I. Mekhtiyeva, J. Optoelectron. Adv. M. **22**(11-12), 596 (2020).

[32] R. Sunil, K. Sushil, P. Aghamkar, S. Sunder, A. Agarwal, J. Magn. Magn. Mater. **323**, 897 (2011).

[33] M. Yarmohammadi, B. D. Hoi, J. Magn. Magn. Mater. **464**, 103 (2018).

[34] K. S. Babu, C. Vijayan, R. Devanathan, Mater. Lett. **58**(7-8), 1223 (2004).

[35] K. C. Preetha, T. L. Remadevi, Mater Sci Semicond Process **16**(3), 605 (2013).

[36] N. Pradhan, D. D. J. Sarma, Phys. Chem. Lett. **2**, 2818 (2011).

[37] P. Wu., J. B. Pan, X. L. Li, X. Hou J. J. Xu, H. Y. Chen, Chem. Eur. J. **21**, 5129 (2015).

[38] R. Chauhan, A. Kumar, R. P. Chaudhary, Appl. Surf. Sci. **270**, 655 (2013).

[39] M. Mahboub, P. Xia, J. B. Van, X. Li, C. H. Lui, M. L. Tang, ACS Energy Letters **3**(4), 767 (2018).

[40] J. Blackburn, D. B. Sulas-Kern, E. M. Miller, Energy Environ. Sci. **13**, 2684 (2020).

[41] T. Kasuya, J. Magn. Magn. Mater. **195**, 141 (1999).

[42] M. Yuan, M. Liu, E. Sargent, Nat. Energy **1**, 16016 (2016).

[43] A. Parveen, S. Agrawal, A. Azam. Opt. Mater. **76**, 21 (2018).

[44] E. Sjosted, L. Nordstrom, D. J. Singh, Solid State Commun. **114**, 15 (2000).

[59] V. I. Anisimov, J. Zaanen, O. K. Andersen, Phys. Rev. B **44**, 943 (1991).

[61] F. D. Murnaghan, Proc. Natl. Acad. Sci. **30**, 244 (1944).

[47] H. J. Monkhorst, J. D. Pack, Phys. Rev. B **13**, 5188 (1976).

[48] P. E. Blochl, O. Jepsen, O. K. Anderson, Phys. Rev. B **49**, 16223 (1994).

[49] O. M. Ozkendir, Adv. J. Chem. B **2**(2), 48 (2020).

[50] B. Merabet, O. M. Ozkendir, A. S. Hassanien, M. A. Maleque, J. Magn. Magn. Mater. **518**, 2021.

[51] A. Walsh, J. L. F. Da-Ilva, S. H. Wei, Phys. Rev. B **78**, 075211 (2008).

[52] D. Kumar, G. Agarwal, B. Tripathi, D. Vyas, V. Kulshrestha, J. Alloy. Compd. **484**, 463 (2009).

[53] A. Carrington, E. A. Yelland, Phys. Rev. B **76**(14), 140508 (2007).

[54] O. K. Andersen, A. I. Liechtenstein, O. Jepsen, F. Paulsen, J. Clin. Eng. **56**, 1573 (1995).

[55] H. Ullah, M. Noor-A-Alam, H. J. Kim, Y. H. Shin, J. Appl. Phys. **124**, 065102 (2018).

[56] L. Turyanska F. Moro, A. N. Knott, M. W. Fay, T. D. Bradshaw, A. Patanè, Part. Part. Syst. Charact. **30**, 945 (2013).

[57] S. Ravishankar, A. R. Balu, K. Usharani, S. Balamurugan, D. Prabha, V. S. Nagarethinam, Optik **134**, 121 (2017).

[58] S. Intachai, C. Suppaso, S. Klinsrisuk, N. Khaorapapong, M. Ogawa, Colloid Surf. A – Physicochem. Eng. ASP **522**, 133 (2017).

_____
*Corresponding author: maleque@iium.edu.my